Nanoscale Research Letters

NANO EXPRESS Open Access

Tumor-Targeted and Biocompatible $MoSe_2$ Nanodots@Albumin Nanospheres as a Dual-Modality Therapy Agent for Synergistic Photothermal Radiotherapy

Feng Qi* and Ruizhen Liu

Abstract

Integrating multiple tumor therapy functions into one nanoplatform has been a new tumor therapy strategy in recent years. Herein, a dual-modality therapy agent consisting of molybdenum selenide nanodots ($MoSe_2$ NDs) and bovine serum albumin (BSA) assembled nanospheres ($MoSe_2$@BSA NSs) was successfully synthesized. After conjugation of folic acid (FA) molecules via polyethylene glycol (PEG) "bridges," the FA-$MoSe_2$@BSA NSs were equipped with tumor-targeting function. The BSA and PEG modifications provided the unstable $MoSe_2$ NDs with excellent physiological stability. Since the end-product FA-$MoSe_2$@BSA NSs had strong near-infrared (NIR) and X-ray absorbance properties, they exhibited good photothermal properties with excellent photothermal stability and radio-sensitization ability, hence, were explored as photothermal radiotherapy agents. In vitro and in vivo experiments indicated that the FA-$MoSe_2$@BSA NSs possessed highly efficient tumor-targeting effect, great biocompability, and synergistic photothermal radiotherapy effect. This work suggests that such biocompatible FA-$MoSe_2$@BSA NSs may be a promising multifunctional dual-modality tumor therapy agent for use in combination tumor therapy.

Keywords: $MoSe_2$, Biocompatibility, Photothermal therapy, Radiotherapy, Dual-modality therapy

Background

Globally, breast cancer occurs at very high incidence rate in women and is notorious for its low survival rate and high rates of metastasis and relapse [1–3]. Surgical resection, radiotherapy (RT), and chemotherapy are commonly used treatment strategies in practice even though these therapies have drawbacks [4]. RT is a highly effective therapy but also harmful to normal tissue. RT has been explored for enhanced therapeutic effect while decreasing its harmful effects. RT employs ionizing radiation (e.g., γ-ray, X-ray) to ionize water molecules into reactive free radicals that damage DNA in cancer cells locally, even in deep region [5]. Since tumor microenvironment was reported to be hypoxic, this was considered as one of the major obstacles for RT [6, 7]. Given these disadvantages, combining RT with other modality therapeutic strategies were reported to be efficient in augmenting the therapeutic effects. To date, photothermal therapy (PTT) has been explored extensively as a minimally invasive cancer treatment due to fewer side effects, high specificity, and minimal side effect to normal tissues [8–15]. However, PTT alone is often insufficient, due to incomplete tumor suppression, especially for the inaccessible tumors, which could potentially cause a tumor relapse [16–18]. Interestingly, PTT was reported to lead to near-infrared (NIR)-induced hyperthermia increasing intratumor blood circulation, and subsequently increased oxygen availability in the tumor microenvironment, causing the cells to be more sensitive to RT [19–21]. Combining RT with PTT could combine the advantages of both which is preferable for improving the therapeutic outcomes of cancer.

Recently, two-dimensional (2D)-layered transition metal dichalcogenides (TMDs), such as MoS_2, WS_2, ReS_2, and so on, have been employed as the NIR adsorbing agents or radio-sensitizers for enhancing the efficacy of PTT or RT due to their physical properties [7, 19, 21]. Shen and

* Correspondence: fengqi_radio@foxmail.com
Department of Radiotherapy, First People's Hospital of Shangqiu City, Shangqiu 476100, China

co-authors have reported a bottom-up preparation of uniform ultrathin ReS_2 nanosheets for image-guided highly effective PTT and RT [21]. In addition to these TMDs, molybdenum selenide ($MoSe_2$) have been reported as a NIR photothermal transducer for PTT [22, 23]. Since PTT alone have its drawback, there is more reason for the exploitation of $MoSe_2$ properties like radio-sensitization for better cancer therapy.

In this work, we first prepared the ultra-small $MoSe_2$ nanodots, which were then assembled with bovine serum albumin (BSA) into nanospheres (NSs) and finally conjugated with tumor-targeting molecule folic acid (FA) via polyethylene glycol (PEG) "bridges." In addition to the great photothermal effect, the obtained FA-$MoSe_2$@BSA NSs were found to have excellent radio-sensitization property. The BSA modification endowed the $MoSe_2$ nanodots (NDs) with excellent physiological stability and biocompability. In vitro and in vivo experiments demonstrated that the FA-$MoSe_2$@BSA NSs exhibited excellent tumor-targeting effect, while simultaneously functioned as NIR photothermal agent and radio-sensitizer for synergistic photothermal radiotherapy with no toxicity to health tissue.

Methods

Materials

FA-PEG_{5000}-NHS and CH_3-PEG_{5000}-NHS were obtained from Shanghai Ponsure Biotech. Co. Ltd. Fluorescein isothiocyanate (FITC), bovine serum albumin (BSA, purified ≥ 98.0%), bulk $MoSe_2$ powder, and Calcein-AM (CA)-propidium iodide (PI) stain were purchased from Sigma-Aldrich (St. Louis, Mo, USA). 4′,6-Diamidino-2-phenylindole (DAPI) were obtained from Aladdin (Shanghai, China). Cell culturing reagents were all provided by Corning Inc. Cell counting kit-8 (CCK-8) was supplied by Dojindo Laboratories (Japan). The γ-H2AX antibody was supplied by Millipore (Temecula, CA).

Preparation of FA-$MoSe_2$@BSA NSs

Firstly, in a typical procedure, 50 mg $MoSe_2$ powder was added into the 25 mL distilled water with 20-min stirring and then was sonicated in an ice-bath by using tip sonication (Scientz-IID, 950 W, 25 kHz). The sonication was pulsed for 2 s on and 3 s off for a total sonication time of 12 h with 70% amplitude. After that, the mixture was centrifuged with 6000 rpm for 25 min. The supernatant was collected and centrifuged again at 12,000 rpm for 30 min, resulting in $MoSe_2$ nanodots ($MoSe_2$ NDs) solution. Afterwards, 25 mg BSA powder were added into the above supernatant with slighted stirring, forming hardened coacervates after stirring for 6 h under 25 °C and pH = 7.4, and then was processed by cross-linking with 0.5% glutaraldehyde (250 μL). Afterwards, the glutaraldehyde was removed by dialyzing in water for 1 day, resulting in the $MoSe_2$@BSA nanospheres ($MoSe_2$@BSA NSs). Next, $MoSe_2$@BSA nanospheres were divided into two parts, the one is mixed with FA-PEG_{5000}-NHS (8 mg), and the other one was mixed with CH_3-PEG_{5000}-NHS (8 mg) solution and stirred for 2 h. At last, the solution was dialyzed in water to result in purified FA-$MoSe_2$@BSA NSs and $MoSe_2$@BSA NSs solution. The prepared solution was stored at 4 °C. In addition, UV-VIS spectrometer was used to quantify the FA on the FA-$MoSe_2$@BSA NSs. In detail, after mixing $MoSe_2$@BSA nanospheres with FA-PEG_{5000}-NHS (8 mg) and reacting for 2 h, the mixture was centrifuged to remove the unbounded FA. The supernate was collected for absorption detection. The FA concentration was detected by a UV–vis spectrometer at FA absorption peak wavelength (280 nm). The FA encapsulation efficiency (EE) was calculated as described in the following equation:

$$\mathrm{EE}\ (\%) = \frac{\mathrm{FA_{total}} - \mathrm{FA_{unloaded}}}{\mathrm{FA_{total}}} \times 100\%$$

Characterizations of FA-$MoSe_2$@BSA NSs

The morphology of the samples was observed by transmission electron microscope (TEM, JEOL JEM2011, Tokyo, Japan) and scanning electron microscope (SEM, Hitachi FE-SEM S-9300, Janpan). Zetasizer (Nano ZS, Malvern Instruments Ltd., UK) was used to the size and zeta potential. The ultraviolet-visible (UV-Vis) absorption spectra were recorded on a UV2550 ultraviolet-visible spectrophotometer (Shimadzu, Kyoto, Japan). The Fourier transform infrared (FTIR) spectra was detected by a FTIR spectrometer (BRUKER VERTEX 70, Ettlingen, Germany). The X-ray powder diffraction (XRD) of the nanospheres was recorded by an X-ray diffractometer (Seifert Jso-Debyerex-2002, Germany). The content of Mo in cells and tissue was measured by inductively coupled plasma-atomic emission spectrometry (ICP-AES, Hitachi P4010, Japan). During NIR irradiation, variation of the temperature was recorded every 30 s using a thermocouple thermometer (Fluke, USA).

Cell Culture and Cellular Uptake

Mouse mammary tumor 4T1 cells were purchased from the American Type Culture Collection (ATCC) and cultured in DMEM media supplemented with 10% FBS and 1% penicillin–streptomycin at 37 °C with 5% CO_2.

For cellular uptake, FITC was used to label the NSs through physical absorption. 4T1 cells adhered to glass slides in 6-well plates and were incubated with free FITC, $MoSe_2$@BSA NSs, FA-$MoSe_2$@BSA NSs + FA, and FA-$MoSe_2$@BSA NSs at the same concentration of FITC (0.05 mg/mL) for 3 h, respectively. The cells were then washed with PBS thrice and fixed by 0.2 mL of glutaraldehyde, followed by staining with DAPI for 10 min. The fluorescence images of cells were captured using the laser scanning microscope. To further observe the

cellular uptake, 4T1 cells (2×10^5 cells/well) were cultured in 6-well cell culture plate for 24 h and then incubated with $MoSe_2$@BSA NSs, FA-$MoSe_2$@BSA NSs + FA, and FA-$MoSe_2$@BSA NSs for extra 3 h. After that, the treated cells were gently washed by PBS for three times, homogenized, and treated with 1 mL aqua regia solution for 4 h. ICP-AES was used to detect the Mo content inside the cells. Uptake ratio = $\frac{Ma}{Mb} \times 100\%$, where Ma is the mass of the Mo inside cells, and Mb is the mass of Mo total added.

In Vitro Biocompatibility

Firstly, health mouse whole blood was collected to detect the in vitro hemolysis of the FA-$MoSe_2$@BSA NSs. In detail, red blood cells (RBCs) were collected by centrifugation. Discarding the supernatants, the collected RBCs were mixed with FA-$MoSe_2$@BSA NSs (in PBS, 1:4) at predetermined concentrations (50 μg/mL, 100 μg/mL, 150 μg/mL, 200 μg/mL, and 400 μg/mL). As positive or negative control, RBCs were incubated with deionized water or PBS. After standing incubated at 37 °C for 1 h, the above set of suspensions were centrifuged (10,000 rpm, 1 min) and the absorbance of the supernatants at 541 nm was monitored by a UV-Vis spectrometer. The hemolysis ratio was calculated using the following equation.

$$\mathrm{HR}\ (\%) = \frac{A_t - A_{nc}}{A_{pc} - A_{nc}} \times 100\%$$

where A_t, A_{pc}, and A_{nc} are the absorbance of the supernatant at 541 nm of the test sample, positive and negative controls, respectively.

In addition, the cytotoxicity of $MoSe_2$@BSA NSs and FA-$MoSe_2$@BSA NSs was detected by a standard CCK-8 assay. 4T1 cells (1×10^5 cells/mL, 0.5 mL) were seeded in 96-well plate and cultured for 24 h. After discarding the old media, fresh media containing 0.01, 0.1, 0.15, 0.3, and 0.4 mg/mL of $MoSe_2$@BSA NSs and FA-$MoSe_2$@BSA NSs were incubated with 4T1 cells for 24 h. PBS was used to mildly wash the cells three times. A 100 μL CCK-8 working solution (10% CCK-8 + 90% DMEM) was then added to each well, followed by incubation at 37 °C for 1 h. The absorbance value at 450 nm was detected using a microplate reader (Labtech, Inc., Durham, North Carolina).

In Vitro Photothermal Radiotherapy

Firstly, the in vitro photothermal performance of the NSs was investigated. $MoSe_2$@BSA NSs and FA-$MoSe_2$@BSA NSs with the same Mo concentrations cultured with cells for 3 h and then irradiated by NIR irradiation for 5 min (808 nm, 1 W/cm^2). The temperature of the treated cells in each well were detected with an infrared thermal camera (Fluke TI25, USA), respectively.

Next, for in vitro photothermal therapy, adherent 4T1 cells were cultured with different concentration of $MoSe_2$@BSA NSs and FA-$MoSe_2$@BSA NSs for 3 h. The NSs outside the cells were removed. The cells were then treated with or without NIR (808 nm, 1 W/cm^2, 5 min) and different dosage of X-ray irradiation (RT, 0–5 Gy, 0.084 Gy/s). After another 24-h incubation, cell viability was detected by a standard CCK-8 assay. The treated cells above were further co-stained by calcein-AM/PI to detect the live and dead cells and then imaged by a confocal laser scanning microscope (calcein-AM: Ex = 488 nm, Em = 515 nm; PI: Ex = 535 nm, Em = 617 nm). Moreover, the treated cells were also analyzed by γ-H2AX immunofluorescence. After the treatment above, the cells were fixed by 4% paraformaldehyde for 10 min and permeabilized with methanol for 15 min at − 20 °C and washed with PBS. Afterwards, the cells were mixed with a blocking buffer (1% BSA in PBS solution) for 1 h at 25 °C and further incubated with anti-phospho-histone γ-H2AX mouse monoclonal antibody (dilution 1:500) overnight at 4 °C. After PBS washing, the fluorescence of the cells was observed by confocal laser scanning microscope.

Animal Model

Balb/c nude mice (5–8-week-old) were provided from Charles River Laboratories (Beijing, China). To establish animal 4T1 tumor model, 150 μL of 10^6 suspension cells were subcutaneous injected into the back of mouse. The mice were fed in animal room and observed every 2 days. All welfare and experimental procedures in this study were performed in accordance with the policies of National Ministry of Health and approved by the Ethics Committee of the First People's Hospital of Shangqiu City. When the tumor volume reached 100 mm^3, the mice were applied for in vivo experiments.

In Vivo Biodistribution and Blood Circulation

Systemic biodistribution of the NSs was investigated in 4T1 tumor-bearing mice. At 1 h, 1 day, 7 days, and 24 days post intravenous injection of $MoSe_2$@BSA NSs and FA-$MoSe_2$@BSA (10 mg/kg), the tumor and major organs (heart, liver, spleen, lung, and kidney) were weighed and digested by aqua regia solution 12 h. The Mo and Se content in these tissues was analyzed by an ICP-AES. In addition, healthy Balb/c mice were intravenously injected with FA-$MoSe_2$@BSA (10 mg/kg). Approximately 10 μL of blood from the tail of mice was collected and analyzed by an ICP-AES for blood circulation.

In Vivo Photothermal Radiotherapy

For in vivo photothermal radiotherapy, tumor-bearing mice ($n = 5$ per group) were treated with PBS + NIR, PBS + RT, $MoSe_2$@BSA NSs + NIR + RT, FA-$MoSe_2$@BSA NSs + RT, FA-$MoSe_2$@BSA NSs + NIR, and FA-$MoSe_2$@BSA NSs + NIR + RT (with 5 mg/kg of $MoSe_2$). The radiotherapy dose was 5 Gy. At 24-h intravenous post injection,

tumor region was irradiated by 5 min NIR irradiation (808 nm, 1 W/cm^2). During the irradiation, the thermal images of the mice were recorded by infrared thermal camera. In the following 30 days, the length and width of the tumor were monitored every 4 days. The relative tumor volume was calculated as V/V_0, where V_0 represents tumor volume when the treatment was initiated. Meanwhile, the body weight of each mouse was also monitored every 4 days.

In Vivo Biocompatibility

For in vivo biocompatibility, 150 μL of FA-$MoSe_2$@BSA NSs (15 mg/kg) was intravenously injected into healthy Balb/c nude mice. Before injection and after 30 days, the blood were collected for complete blood counts evaluations including white blood cell (WBC), red blood cells (RBC), hemoglobin (HGB), mean platelet volume (MPV), mean corpuscular hemoglobin (MCH), hematocrit (HCT), mean corpuscular hemoglobin concentration (MCHC), mean corpuscular volume (MCV), and platelet (PLT). At the same time, the mice were sacrificed and the heart, liver, spleen, lung, and kidney were collected. The obtained organs were fixed with 4% paraformaldehyde and sectioned into 5 μm slices and stained with hematoxylin and eosin (H&E). The stained sections were imaged by a digital microscope.

Statistical Analysis

Data were shown as mean ± SD. Two-tailed Student's *t* test was used to analyze the statistical significance of two groups. The differences were considered significant for $^*P < 0.05$ and highly significant for $^{**}P < 0.01$.

Results and Discussion

Preparation and Characterization of FA-$MoSe_2$@BSA NSs

The preparation procedure of the FA-$MoSe_2$@BSA NSs is depicted in Fig. 1a. Briefly, unstable $MoSe_2$ nanodots were prepared from bulk $MoSe_2$ under ultrasonication, then stabilized and assembled by BSA protein, and conjugated simultaneously to the target molecule FA via PEG "bridges." The prepared $MoSe_2$ NDs were ultra-small nanodots as observed in TEM (Fig. 1b). The XRD pattern of $MoSe_2$ NDs was shown in Additional file 1: Figure S1. The diffraction peak at 13.1° belongs to the (002) plane, matching the peak position of bulk $MoSe_2$. The distinct (002) peak indicates the existence of few-layers in the c-axis of $MoSe_2$ NDs. The diffraction peak of (100) plane for $MoSe_2$ NDs broadens significantly in comparison with bulk $MoSe_2$, which may originate from the size reduction of $MoSe_2$ NDs [23]. Following assembly and conjugation with BSA protein and FA, the nanocomposites formed sphere-like particles (Fig. 1c). The FTIR spectra showed the existence of –CONH- bond in FA-$MoSe_2$@BSA NSs, indicating that FA was likely conjugated onto $MoSe_2$ through ester bond

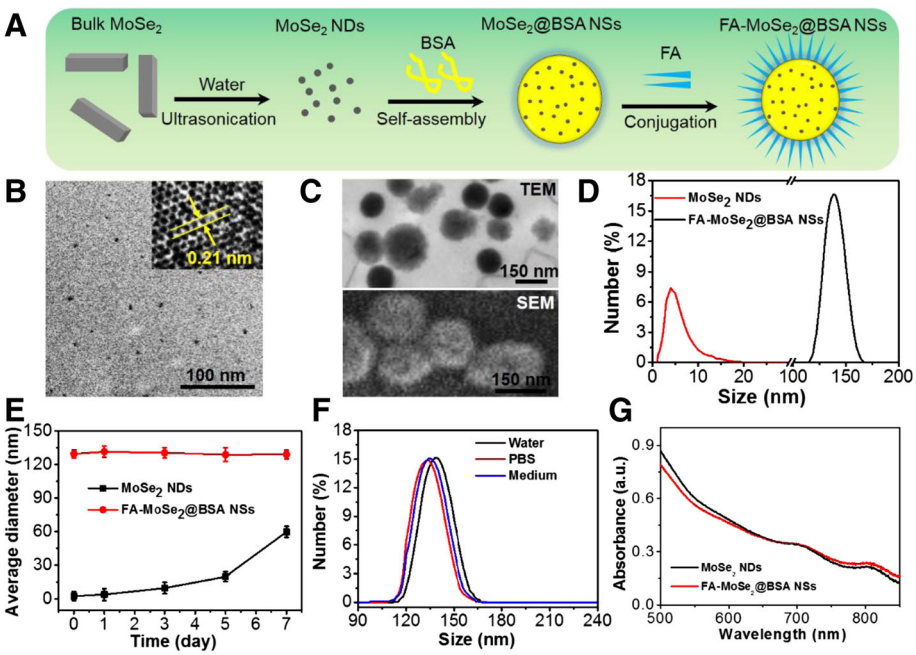

Fig. 1 **a** A schematic of FA-$MoSe_2$@BSA NSs synthesis. **b** TEM image of $MoSe_2$ NDs. Inset was the high-resolution TEM image. **c** The TEM and SEM images of FA-$MoSe_2$@BSA NSs. **d** The size distribution of $MoSe_2$ NDs and FA-$MoSe_2$@BSA NSs. **e** The size change of $MoSe_2$ NDs and FA-$MoSe_2$@BSA NSs in water over 7 days. **f** The size distribution of FA-$MoSe_2$@BSA NSs in water, PBS, and medium, respectively. **g** The absorbance spectra of $MoSe_2$ NDs and FA-$MoSe_2$@BSA NSs

(Additional file 1: Figure S2). In addition, we have quantified the FA on the FA-$MoSe_2$@BSA nanospheres, which was 10.5 ± 0.11%. DLS analysis revealed that the average diameters of $MoSe_2$ NDs and FA-$MoSe_2$@BSA NSs were approximately 3.8 nm and 139.8 nm, respectively (Fig. 1d). After 7 days of storage, the size of $MoSe_2$ NDs increased from 3.8 to 63.2 nm, while FA-$MoSe_2$@BSA NSs showed no obvious change in size (Fig. 1e), indicating aggregation and the low stability of $MoSe_2$ NDs in long-term storage. In addition, when dispersed in different media like water, PBS, and cell medium, FA-$MoSe_2$@BSA NSs displayed similar size distribution (Fig. 1f). These results indicated the FA-$MoSe_2$@BSA NSs are stable in physiological conditions and this improved stability of $MoSe_2$ NDs is likely attributed to BSA assembly and PEG coating [24, 25]. As shown in Fig. 1g, the ultraviolet-visible (UV-Vis) spectra of $MoSe_2$ NDs and FA-$MoSe_2$@BSA NSs had similarly high NIR absorbance characteristics, indicating that the BSA and FA modifications did not affect the absorbance of $MoSe_2$.

Photothermal Effect of FA-$MoSe_2$@BSA NSs

Figure 2a shows that the temperature of FA-$MoSe_2$@BSA NSs solution increased with increasing concentrations (0–200 μg/mL). After NIR irradiation (808 nm, 1 W/cm^2) for 5 min, the temperature change of FA-$MoSe_2$@BSA NSs solution at 200 μg/mL reached approximately 41 °C, while the temperature of pure water only increased by approximately 1.5 °C under the same conditions. Moreover, the temperature change of FA-$MoSe_2$@BSA NSs irradiated under different power intensity (0.5–2.0 W/cm^2) for 5 min was also recorded. As shown in Fig. 2b, the temperature increased to a maximum of 40.6 °C with increasing laser power intensity. Figure 2c depicts the photostability of FA-$MoSe_2$@BSA NSs, implying that the FA-$MoSe_2$@BSA NSs retained its excellent photothermal effects without any attenuation of the temperature elevation after three cycles of NIR irradiation. These results demonstrated that FA-$MoSe_2$@BSA NSs had significant photostability and excellent photothermal properties. As shown in Fig. 2d, the Hounsfield unit (HU) values of FA-$MoSe_2$@BSA NSs images obtained with computed tomography (CT) were positively correlated with their concentrations, indicating the NSs could potentially be used as a radio-sensitizer.

Cellular Uptake and In Vitro Biocompatibility

To evaluate the cellular uptake, $MoSe_2$@BSA NSs and FA-$MoSe_2$@BSA NSs were labeled by FITC. As depicted in Fig. 3a, much stronger FITC fluorescence was observed inside the cytoplasm in FA-$MoSe_2$@BSA NSs-treated cells, compared to that of $MoSe_2$@BSA

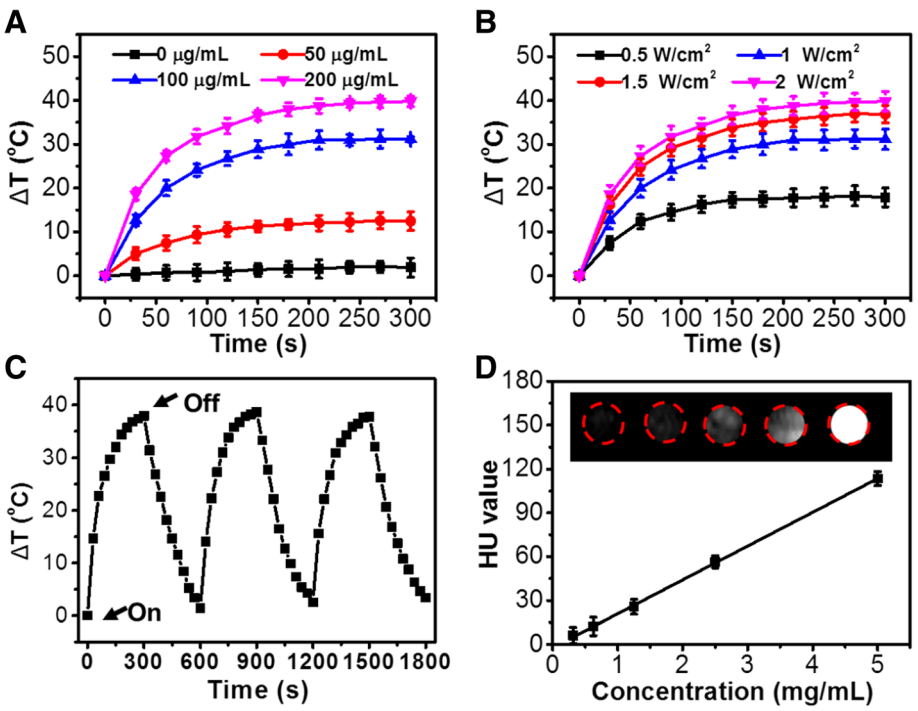

Fig. 2 **a** Photothermal heating curves of FA-$MoSe_2$@BSA NSs solution at different concentrations (0, 50, 100, and 200 μg/mL) under 808 nm laser irradiation at the power density of 1 W/cm^2. **b** Photothermal heating curves of FA-$MoSe_2$@BSA NSs solution at 100 μg/mL under 808 nm laser irradiation at different power density (0.5, 1, 1.5, and 2 W/cm^2). **c** Temperature variations of FA-$MoSe_2$@BSA NSs under three cycles of 808 nm laser irradiation at the power density of 1 W/cm^2. **d** CT images (inset) and HU values of FA-$MoSe_2$@BSA NSs with different concentrations

NSs- and free FITC-treated cells. ICP-AES quantitative analysis showed higher cellular uptake of FA-$MoSe_2$@BSA NSs than $MoSe_2$@BSA NSs (Fig. 3b). These results demonstrated that FA enhanced the cellular uptake of FA-$MoSe_2$@BSA NSs. Interestingly, after an FA blocking, the FA-$MoSe_2$@BSA NSs-treated cells showed weaker green FITC fluorescence inside the cytoplasm compared with that of without FA blocking. Corresponding, the cell uptake rate of FA-$MoSe_2$@BSA NSs + FA-treated cells is less than that of FA-$MoSe_2$@BSA NSs-treated cells. It indicates that the FA receptor on the cell membrane is hindered (by free FA), in turn, reduces the targeting ability and accessibility of FA-$MoSe_2$@BSA NSs. It further demonstrates that FA receptor is over expressed in 4T1 cells and FA-MoSe2@BSA NSs enter cells probably through a receptor-mediated endocytosis pathway [26, 27].

The in vitro biocompability of the NSs was evaluated by hemolysis and cytotoxicity analyses. Figure 4a showed no obvious hemolysis for FA-$MoSe_2$@BSA NSs-treated red blood cells (RBCs) or PBS-treated RBCs. Moreover, when concentrations of up to 0.4 mg/mL of $MoSe_2$@BSA NSs and FA-$MoSe_2$@BSA NSs were incubated with cells for 24 h, there were less than 10% viability suppression. These results suggested that the FA-$MoSe_2$@BSA NSs have great in vitro biocompatibility.

In Vitro Photothermal Radiotherapy

As shown in Fig. 5a, b, cells treated with FA-$MoSe_2$@BSA NSs showed the highest temperature increase ($\Delta T = 23.6$ °C) after 5 min of NIR irradiation (808 nm, 1 W/cm^2) compared to $MoSe_2$@BSA NSs- and PBS-treated cells. Figure 5c showed an enhancement of RT efficacy by addition of FA-$MoSe_2$@BSA NSs. With increasing X-ray doses, the RT efficacy of FA-$MoSe_2$@BSA NSs improved much more than that of $MoSe_2$@BSA NSs. It was demonstrated that FA-$MoSe_2$@BSA NSs could enhance radiotherapy effect, probably due to their X-ray attenuation capability that could concentrate X-ray radiation energy inside tumor cells and generate secondary Auger electrons, resulting in DNA damage and suppression of cell growth [28, 29].

For further evaluation of combined RT and PTT therapeutic effect, 4T1 cells were treated with only NIR or RT, FA-$MoSe_2$@BSA NSs + RT, FA-$MoSe_2$@BSA NSs + NIR, or FA-$MoSe_2$@BSA NSs + NIR + RT. As shown in Fig. 5d, FA-$MoSe_2$@BSA NSs + NIR + RT-treated group displayed the most significant concentration-dependent cell death, with 92.8% suppression rate. The excellent therapeutic effect of the FA-$MoSe_2$@BSA NSs was likely due to (1) the photothermal ablation of PTT and DNA damage by RT of FA-$MoSe_2$@BSA NSs, and (2) FA targeting enhanced the cell internalization of FA-$MoSe_2$@BSA NSs and thus the generation of more heat and X-ray to kill the cells.

As shown in Fig. 6a, few dead cells could be observed in the PBS + NIR and PBS + RT control groups. Even though dead cells were found in FA-$MoSe_2$@BSA NSs + RT or FA-$MoSe_2$@BSA NSs + NIR groups, but living cells still existed. Conversely, in the FA-$MoSe_2$@BSA NSs + NIR + RT group, more than 95% of cells were damaged and showed red fluorescence, indicating that combined RT and PTT

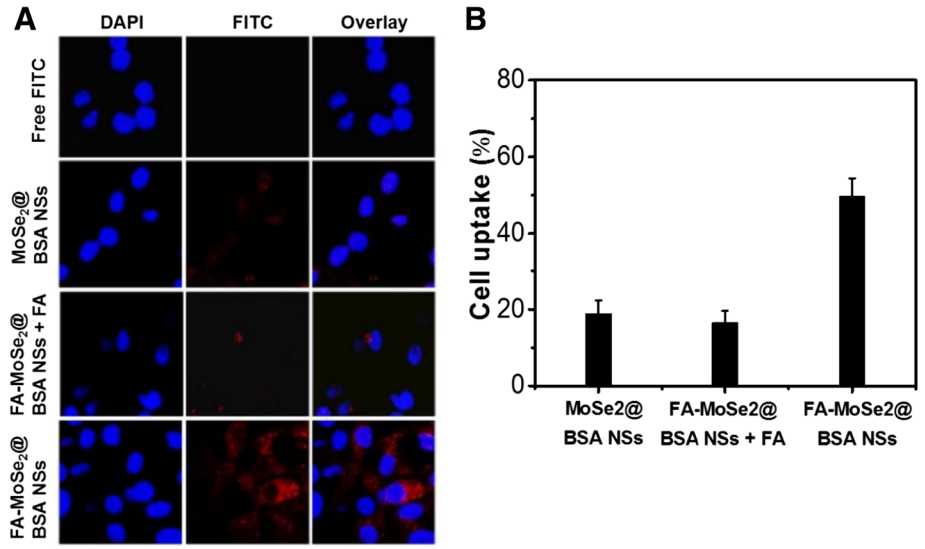

Fig. 3 **a** Confocal fluorescence images of 4T1 cells after incubation with free FITC, and FITC-labeled $MoSe_2$@BSA NSs, FA-$MoSe_2$@BSA NSs + FA blocking, and FA-$MoSe_2$@BSA NSs. Red and blue colors represent FITC fluorescence and DAPI stained cell nuclei, respectively. **b** ICP-AES quantitative analysis of 4T1 cells toward $MoSe_2$@BSA NSs, FA-$MoSe_2$@BSA NSs + FA blocking, and FA-$MoSe_2$@BSA NSs

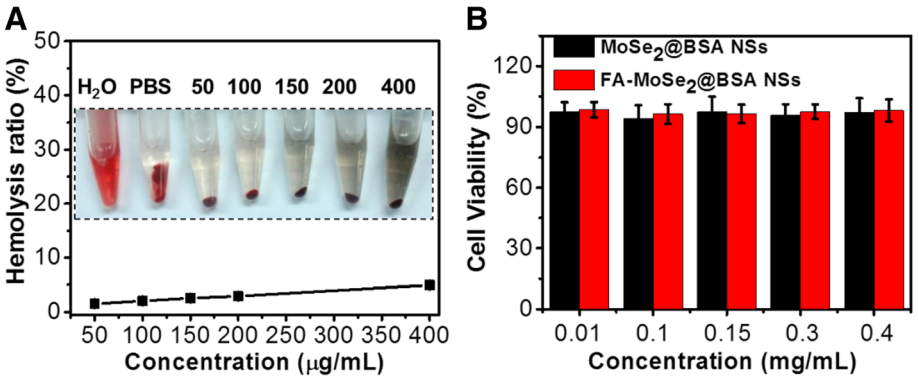

Fig. 4 a Hemolysis ratio of RBCs after 1-h incubation with FA-$MoSe_2$@BSA NSs at different concentrations. The inset shows the photograph of RBCs exposed to distilled water, PBS, and FA-$MoSe_2$@BSA NSs with different concentrations followed by centrifugation. **b** Cell viability of 4T1 cells after treatment with towards $MoSe_2$@BSA NSs and FA-$MoSe_2$@BSA NSs at different concentrations for 24 h

of FA-$MoSe_2$@BSA NSs could enhance the therapeutic efficiency.

Since FA-$MoSe_2$@BSA NSs have high X-ray absorbance, it would be potential to have the capability to enhance RT. As shown in Fig. 6b, very low levels of γ-H2AX signals were observed in the PBS-treated groups, FA-$MoSe_2$@BSA NSs only, and FA-$MoSe_2$@BSA NSs + NIR-treated groups. Meanwhile, FA-$MoSe_2$@BSA NSs + NIR + RT-treated group showed higher levels of γ-H2AX signals, indicating more significant DNA damage inside cell nuclei. These results demonstrated that FA-$MoSe_2$@BSA NSs could enhance RT effect attributing to its X-ray attenuation capability, which would concentrate X-ray radiation energy inside tumor cells and generate secondary and Auger electrons to cause DNA damages and suppression of cell growth [30–32].

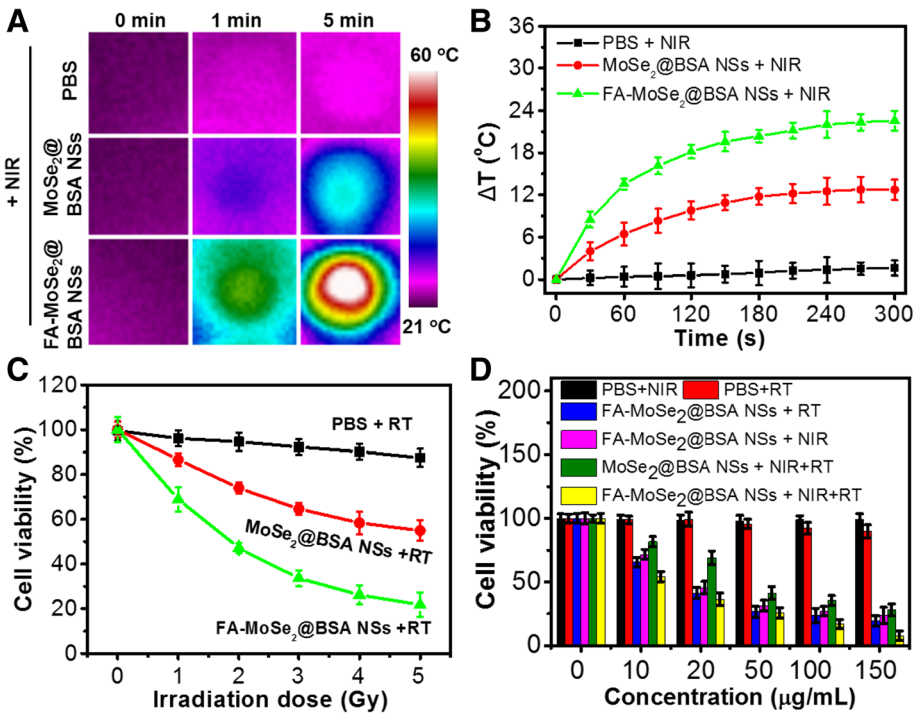

Fig. 5 a Thermal images of PBS, $MoSe_2$@BSA NSs and FA-$MoSe_2$@BSA NSs treated cells, and **b** the corresponding temperature change curves under continuous irradiation with an 808 nm laser (1 W/cm^2). **c** Cell viability of 4 T1 cells treated with PBS, $MoSe_2$@BSA NSs, and FA-$MoSe_2$@BSA NSs combined with different dose of X-ray irradiation (0–5 Gy). **d** Cell viability of 4T1 cells treated with different samples under 808 nm NIR laser (5 min, 1 W/cm^2) and X-ray (5 Gy) irradiation

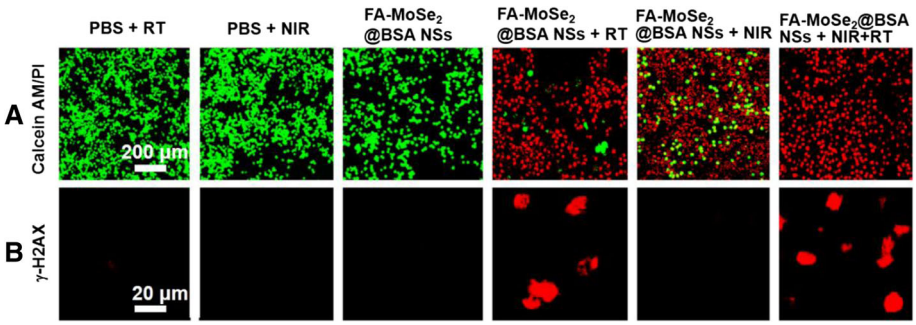

Fig. 6 **a** Live–dead and **b** γ-H2AX staining images of 4T1 cells treated with PBS + RT, PBS + NIR, FA-$MoSe_2$@BSA NSs, FA-$MoSe_2$@BSA NSs + NIR, FA-$MoSe_2$@BSA NSs + RT, and FA-$MoSe_2$@BSA NSs + NIR + RT, respectively

In Vivo Biodistribution and Blood Circulation

As shown in Fig. 7a, b, at 24-h post-injection, the Mo and Se elements accumulated in the tumor except for liver and kidney. The contents of Mo elements in tumor tissue post-injections of $MoSe_2$@BSA NSs and FA-$MoSe_2$@BSA NSs were also evaluated. As shown in Fig. 7c, the Mo levels in tumor tissue for FA-$MoSe_2$@BSA NSs-treated group increased with time and reached the peak at 24-h post-injection, which was higher than that of $MoSe_2$@BSA NSs-treated group. Figure 7d shows the blood circulation curve of Mo at different time point post-injection of FA-$MoSe_2$@BSA NSs. The Mo $t_{1/2}\alpha$ (blood distribution half-life) and $t_{1/2}\beta$ (blood terminal elimination half-life) of the FA-$MoSe_2$@BSA NSs group are 0.91 ± 0.06 h and 16.96 ± 1.3 h, respectively. These results were likely due to (1) prolonged blood circulation promoted by PEG and BSA modifications [24, 33], (2) decreased macrophage clearance of nanoparticles by the reticuloendothelial system [34, 35], and (3) facilitated tumor targeting effect by the FA modification and subsequent accumulation in

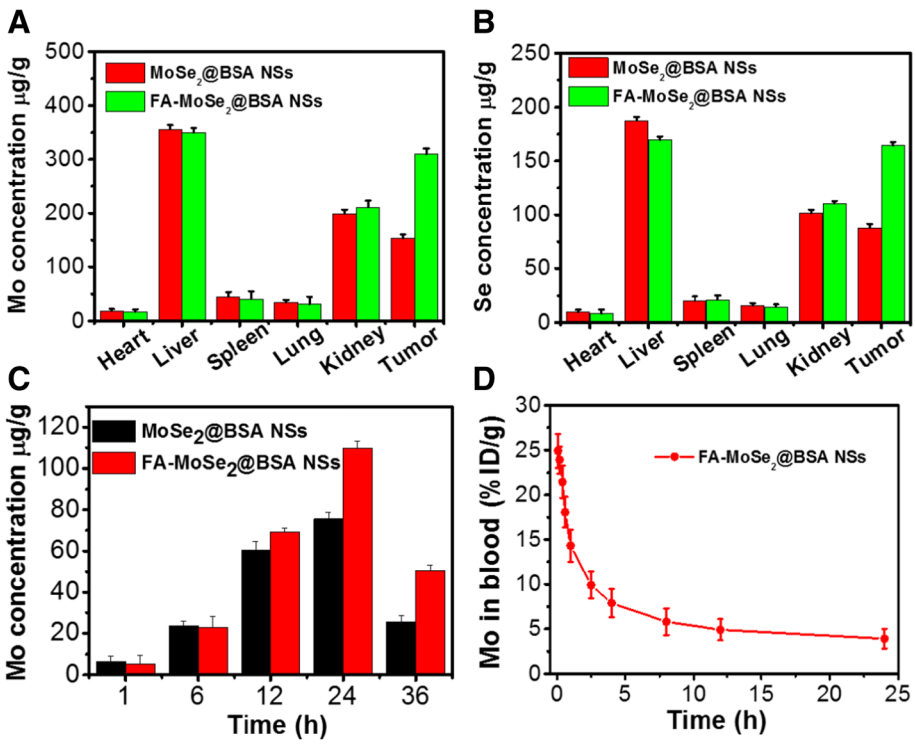

Fig. 7 The **a** Mo and **b** Se elements content of tumor and major organs including heart, liver, spleen, lung, and kidney in $MoSe_2$@BSA NSs and FA-$MoSe_2$@BSA NSs-treated mice. **c** Quantitative in vivo analysis of the Mo elements content of the tumor regions in $MoSe_2$@BSA NSs and FA-$MoSe_2$@BSA NSs-treated mice as a function of injection time. **d** Blood circulation curve of Mo at different time points post-injection of FA-$MoSe_2$@BSA NSs

tumor tissues. The tumor optimum accumulation time of FA-$MoSe_2$@BSA NSs could guide the in vivo photothermal radiotherapy.

In Vivo Photothermal Radiotherapy

As shown in Fig. 8a, b, the temperature of the tumor region under NIR irradiation (5 min, 1 W/cm^2) showed about 22.1 °C increase at 24-h post-injection of FA-$MoSe_2$@BSA NSs, compared with that of PBS- or $MoSe_2$@BSA NSs-treated groups. This indicated that FA-$MoSe_2$@BSA NSs have excellent photothermal effect in vivo. As shown in Fig. 8c, no distinct weight changes were observed in the control or any of the treated Balb/c mice during the 30-day treatment duration, demonstrating that the treatments did not affect the health of these mice. Next, 4T1-tumor-bearing mice were randomly divided into six groups. Group 1: NIR; group 2: RT; group 3: FA-$MoSe_2$@BSA NSs + RT; group 4: FA-$MoSe_2$@BSA NSs + NIR; group 5: $MoSe_2$@BSA NSs + NIR + RT; and group 6: FA-$MoSe_2$@BSA NSs + NIR + RT. Then, 5 mg/kg of $MoSe_2$ was used in all groups. The radiotherapy dose was 5 Gy, and the dose rate is 0.084 Gy/s. At 24-h intravenous post injection, tumor region was irradiated by 5 min NIR irradiation (808 nm, 1 W/cm^2). The tumor sizes were closely monitored afterward (Fig. 8d). Compared to other groups, the most remarkable tumor growth inhibition was observed in group 6 after the combined photothermal-radiotherapy with FA-$MoSe_2$@BSA NSs, achieving an obvious synergistic therapeutic outcome in comparison to PTT alone or RT alone delivered by FA-$MoSe_2$@BSA NSs (Fig. 8d).

In Vivo Biocompatibility

As a kind of nanoagent for in vivo biomedical applications, their potential toxic side effect is something that always requires particular attention. In addition to the body weight data of mice in different groups post various treatments in Fig. 8c, the H&E staining images of major organs and complete blood panel assays were provided to evaluate the safety of the FA-$MoSe_2$@BSA NSs. As shown using H&E staining in Fig. 9a, no apparent pathological tissue damage or abnormality in major organs (heart, liver, spleen, lung, and kidney) was observed in FA-$MoSe_2$@BSA NSs-treated mice. Moreover, as illustrated in Fig. 9b, the parameters of WBC, RBC, HGB, MCH, HCT, MCHC, MCV, and PLT for FA-$MoSe_2$@BSA NSs-treated mice were within the normal range. These results demonstrated that FA-$MoSe_2$@BSA NSs exhibited low toxicity and excellent in vivo biocompatibility.

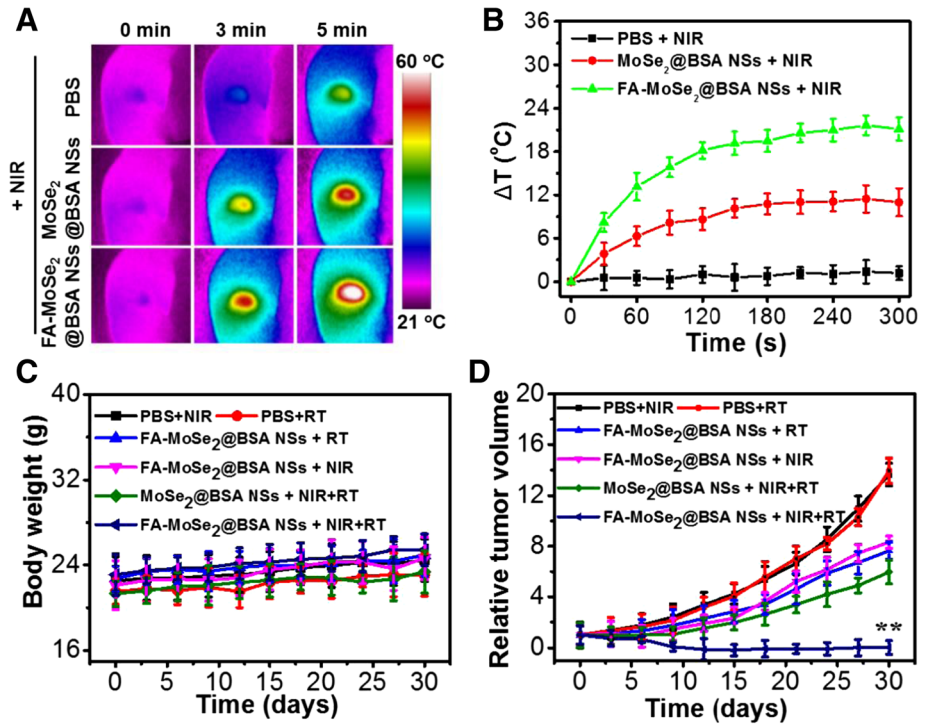

Fig. 8 a In vivo thermal images of mouse after intravenous injection of saline, $MoSe_2$@BSA NSs and FA-$MoSe_2$@BSA NSs and durations NIR irradiation (808 nm, 1 W/cm^2). **b** The corresponding temperature change curves of tumor regions in mice. **c** The weight and **d** relative tumor volume profile of 4T1 xenografted tumors after intravenous injection of PBS + RT, PBS + NIR, FA-$MoSe_2$@BSA NSs + NIR, FA-$MoSe_2$@BSA NSs + RT, $MoSe_2$@BSA NSs + NIR + RT, and FA-$MoSe_2$@BSA NSs + NIR + RT, respectively. $^{**}P < 0.01$ vs control group and other groups

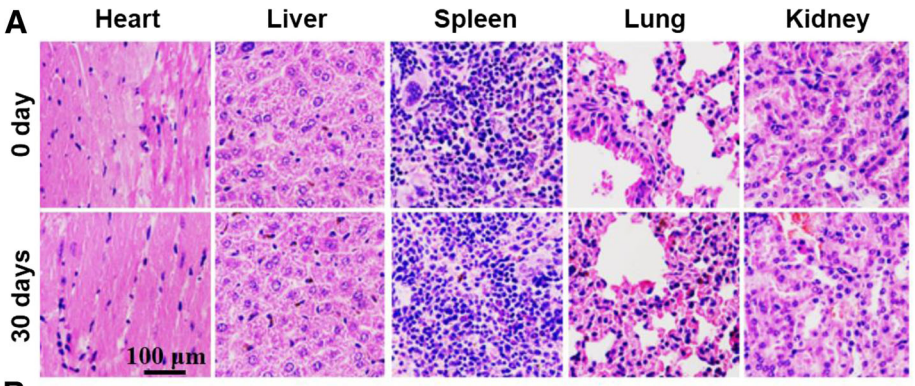

B

	WBC (10^9/L)	RBC (10^{12}/L)	HGB (g/L)	MCH (pg)
Reference range	5.69-14.84	8.16-11.69	124-189	13-17.6
0 day	9.85±0.68	11.21±0.45	168.42±8.96	15.36±0.48
30 days	8.52±0.77	9.99±0.38	147.63±7.99	15.82±0.83
	HCT (%)	MCHC (g/L)	MCV (fL)	PLT (10^9/L)
Reference range	43-67	239-331	50.8-64.1	476-1611
0 day	51.65±1.23	279.1±9.56	53.12±0.93	1021.8±63.2
30 days	48.12±1.12	301.4±10.1	56.51±0.77	1204.6±49.6

Fig. 9 a H&E-stained tissue sections of major organs, including the heart, liver, spleen, lung, and kidney from mice treated with FA-$MoSe_2$@BSA NSs at day 0 and day 30 (scale bar = 100 μm). **b** Blood biochemistry of mice at days 0 and 30 post-treatment with FA-$MoSe_2$@BSA NSs

Conclusions

In summary, MoSe2 NDs was first prepared by ultrasonication, and $MoSe_2$@BSA nanospheres was then successfully synthesized via a simple BSA self-assembly method. The BSA surface provided a rich modifiable functional group that readily conjugated FA molecules, enabling the synthesis of versatile FA-$MoSe_2$@BSA NSs which showed outstanding physiological stability and excellent tumor targeting effect. Due to the strong radio-sensitization ability and high NIR absorption of $MoSe_2$ NDs, FA-$MoSe_2$@BSA NSs could be used as a photothermal agent for NIR-induced tumor ablation, and act as a radio-sensitizer to enhance the efficacy of RT. In vitro and in vivo experiments verified that FA-$MoSe_2$@BSA NSs exhibited high cytotoxicity under NIR and X-ray irradiation, contributing to remarkably enhanced therapeutic effect in the tumor-targeted combined photothermal-radiotherapy. Most importantly, it was demonstrated that FA-$MoSe_2$@BSA NSs have great biocompability in vitro and in vivo, encouraging further biomedical or clinic applications. Therefore, considering all the above desirable characteristics, the FA-$MoSe_2$@BSA NSs with highly integrated functionalities is promising for applications in cancer therapy.

Additional File

Additional file 1: Figure S1. XRD pattern of bulk $MoSe_2$ and $MoSe_2$ NDs. Figure S2. FTIR spectra of FA-$MoSe_2$@BSA NSs. (DOCX 145 kb)

Abbreviations

BSA: Bovine serum albumin; FA: Folic acid; $MoSe_2$: Molybdenum selenide; NDs: Nanodots; NIR: Near infrared; NSs: Nanospheres; PEG: Polyethylene glycol; PTT: Photothermal therapy; RT: Radiotherapy

Funding

Not applicable.

Availability of Data and Materials

The conclusions made in this manuscript are based on the data (main text and figures) presented and shown in this paper.

Authors' Contributions

FQ and RL designed the experiment and analyzed the data. FQ conducted the experiments and prepared the manuscript. FQ and RL revised and approved the manuscript.

Competing Interests

The authors declare that they have no competing interests.

Publisher's Note

Received: 12 November 2018 Accepted: 11 February 2019
Published online: 26 February 2019

References

1. Deng C et al (2018) Co-administration of biocompatible self-assembled polylactic acid–hyaluronic acid block copolymer nanoparticles with tumor-penetrating peptide-iRGD for metastatic breast cancer therapy. J Mater Chem B 6:3163–3180
2. Yates LR et al (2017) Genomic evolution of breast cancer metastasis and relapse. Cancer Cell 32:169–184
3. Schiavon G et al (2015) Analysis of ESR1 mutation in circulating tumor DNA demonstrates evolution during therapy for metastatic breast cancer. Sci Transl Med 7:313ra182
4. Miller KD et al (2016) Cancer treatment and survivorship statistics, 2016. CA-Cancer J Clin 66:271–289
5. Deng J et al (2018) Tumor targeted, stealthy and degradable bismuth nanoparticles for enhanced X-ray radiation therapy of breast cancer. Biomaterials 154:24–33
6. Wardman P (2007) Chemical radiosensitizers for use in radiotherapy. Clin Oncol 19:397–417
7. Wang J et al (2016) MoS_2 quantum dot@ polyaniline inorganic–organic nanohybrids for *in vivo* dual-modal imaging guided synergistic photothermal/radiation therapy. ACS Appl Mater Inter 8:24331–24338
8. Huang X et al (2006) Cancer cell imaging and photothermal therapy in the near-infrared region by using gold nanorods. J Am Chem Soc 128:2115–2120
9. Robinson JT et al (2011) Ultrasmall reduced graphene oxide with high near-infrared absorbance for photothermal therapy. J Am Chem Soc 133:6825–6831
10. Chen J et al (2014) One-step reduction and PEGylation of graphene oxide for photothermally controlled drug delivery. Biomaterials 35:4986–4995
11. Miao Z et al (2018) Surface-bioengineered gold nanoparticles for biomedical applications. Curr Med Chem 25:1920–1944
12. Liu W et al (2019) Reduced graphene oxide (rGO) hybridized hydrogel as a near-infrared (NIR)/pH dual-responsive platform for combined chemo-photothermal therapy. J Colloid Interface Sci 536:160–170
13. Chen H et al (2018) 2D transition metal dichalcogenide nanosheets for photo/thermo-based tumor imaging and therapy. Nanoscale Horiz 3:74–89
14. Yu X et al (2017) Fabrication technologies and sensing applications of graphene-based composite films: advances and challenges. Biosens Bioelectron 89:72–84
15. Zhao X et al (2015) Recent advances in the fabrication and structure-specific applications of graphene-based inorganic hybrid membranes. Nanoscale 7:5080–5093
16. Yang H et al (2018) Artesunate-loaded and near-infrared dye-conjugated albumin nanoparticles as high-efficiency tumor-targeted photo-chemo theranostic agent. Nanoscale Res Lett 13:319
17. Kuthala N et al (2017) Engineering novel targeted boron-10-enriched theranostic nanomedicine to combat against murine brain tumors via MR imaging-guided boron neutron capture therapy. Adv Mater 29:1700850
18. Ayala-Orozco C et al (2014) Sub-100nm gold nanomatryoshkas improve photo-thermal therapy efficacy in large and highly aggressive triple negative breast tumors. J Control Release 191:90–97
19. Cheng L et al (2015) Bottom-up synthesis of metal-ion-doped WS2 nanoflakes for cancer theranostics. ACS Nano 9:11090–11101
20. Xiaoyan C et al (2015) Radionuclide ^{131}I labeled reduced graphene oxide for nuclear imaging guided combined radio-and photothermal therapy of cancer. Biomaterials 66:21–28
21. Shen S et al (2017) Bottom-up preparation of uniform ultrathin rhenium disulfide nanosheets for image-guided photothermal radiotherapy. Adv Funct Mater 27:1700250
22. Chen J et al (2018) Hybrid $MoSe_2$–indocyanine green nanosheets as a highly efficient phototheranostic agent for photoacoustic imaging guided photothermal cancer therapy. Biomater Sci 6:1503–1516
23. Yuwen L et al (2016) Aqueous phase preparation of ultrasmall $MoSe_2$ nanodots for efficient photothermal therapy of cancer cells. Nanoscale 8:2720–2726
24. Geng T et al (2017) Resveratrol-loaded albumin nanoparticles with prolonged blood circulation and improved biocompatibility for highly effective targeted pancreatic tumor therapy. Nanoscale Res Lett 12:437
25. Deng W et al (2018) Development of biocompatible and VEGF-targeted paclitaxel nanodrugs on albumin and graphene oxide dual-carrier for photothermal-triggered drug delivery *in vitro* and *in vivo*. Int J Nanomedicine 13:439
26. Jones SK et al (2017) Revisiting the value of competition assays in folate receptor-mediated drug delivery. Biomaterials 138:35–45
27. Suen WLL et al (2014) Size-dependent internalisation of folate-decorated nanoparticles via the pathways of clathrin and caveolae-mediated endocytosis in ARPE-19 cells. J Pharm Pharmacol 66:564–573
28. Siva S et al (2016) Radiotherapy for non–small cell lung cancer induces DNA damage response in both irradiated and out-of-field normal tissues. Clin Cancer Res 22:4817–4826
29. Goldstein M et al (2015) The DNA damage response: implications for tumor responses to radiation and chemotherapy. Annu Rev Med 66:129–143
30. Friedland W et al (2017) Comprehensive track-structure based evaluation of DNA damage by light ions from radiotherapy-relevant energies down to stopping. Sci Rep 7:45161
31. Turinetto V et al (2015) Multiple facets of histone variant H2AX: a DNA double-strand-break marker with several biological functions. Nucleic Acids Res 43:2489–2498
32. Song G et al (2016) Perfluorocarbon-loaded hollow Bi_2Se_3 nanoparticles for timely supply of oxygen under near-infrared light to enhance the radiotherapy of cancer. Adv Mater 28:2716–2723
33. Mima Y et al (2015) Anti-PEG IgM is a major contributor to the accelerated blood clearance of polyethylene glycol-conjugated protein. Mol Pharm 12:2429–2435
34. Gómez-Vallejo V et al (2018) PEG-copolymer-coated iron oxide nanoparticles that avoid the reticuloendothelial system and act as kidney MRI contrast agents. Nanoscale 10:14153–14164
35. Chung EJ et al (2015) *In vivo* biodistribution and clearance of peptide amphiphile micelles. Nanomedicine 11:479–487